**Title:** Effect of Oxygen Partial Pressure and $B_2O_3$ on Crystallization Behavior of Phosphorus- and Iron-Containing Phases in a $CaO$-$SiO_2$-$Fe_2O_3$-$P_2O_5$ melt

**Authors**: JUNCHENG LI, GUOXUAN LI, JINSHAN LIANG, DONG GUAN, JINGWEI LI, YANLING ZHANG, SHAOWEN WU, SEETHARAMAN SRIDHAR and ZUSHU LI

**Mailing address:** School of Material Science and Engineering, Jiangsu University, Zhenjiang, Jiangsu Province, 212013 P. R. China

**Corresponding author:** JUNCHENG LI

**Abstract:**

JUNCHENG LI, is Professor with School of Material Science and Engineering, Jiangsu University, Zhenjiang, Jiangsu Province, 212013 P. R. China. GUOXUAN LI, JINSHAN LIANG and DONG GUAN are master students with School of Material Science and Engineering, Jiangsu University, Zhenjiang, Jiangsu Province, 212013 P. R. China. JINGWEI LI, is Professor with School of Materials Science and Engineering, Hefei University of Technology, Anhui, 230009, China. YANLING ZHANG is Professor with State Key Laboratory of Advanced Metallurgy, University of Science and Technology Beijing, Beijing, 100083, China. SHAOWEN WU is a PhD student with State Key Laboratory of Advanced Metallurgy, University of Science and Technology Beijing, Beijing, 100083, China. SEETHARAMAN SRIDHAR, is Professor with School for Engineering of Matter, Transport and Energy, Arizona State University Tempe, AZ 85287, USA. ZUSHU LI, is Professor with WMG, the University of Warwick, Coventry, CV4 7AL, UK.
Contact e-mail: leejc2011@163.com.

To help maintain the sustainability of the steel industry by improving slag utilization, we are developing a novel process to recover P and Fe from steelmaking slag by controlling oxygen partial pressure and adding slag modifier $B_2O_3$, to control the precipitation of targeted phases. In this paper, the precipitated phases of the molten synthetic CaO-$SiO_2$-FeO-$P_2O_5$(-$B_2O_3$) slags were predicted through thermodynamic calculations using FactSage 8.1. A confocal laser scanning microscope (CLSM) was used to in-situ observe the crystallization behavior of the targeted metal oxides in the slags. It was found that iron and phosphorus could be recovered in the form of magnetite ($Fe_3O_4$) and calcium phosphate ($Ca_{10}P_6O_{25}$) phases by controlling oxygen partial pressure and adding slag modifier $B_2O_3$. By changing oxygen partial pressure from 0.21 to $10^{-6}$ atm, the iron-containing phase transformed from $Ca_2Fe_2O_5$ to magnetite ($Fe_3O_4$). Through the introduction of $B_2O_3$ from 2% to 8%, the amount of calcium phosphate ($Ca_{10}P_6O_{25}$) first increased and then decreased, with the maximum of 28% (e.g. 28 g /100 g slag studied) at 6% $B_2O_3$.

**Key Words:** Steelmaking slags; Oxygen partial pressure; $B_2O_3$; Modification; Magnetite ($Fe_3O_4$); Calcium phosphate ($Ca_{10}P_6O_{25}$)

## 1. Introduction

Steelmaking slag, about 15% of the crude steel output, is the primary solid waste in the steel industry [1, 2]. During the steelmaking process, the slag is crucial for steel chemistry control and thermal insulation. Amongst the key reactions in the steelmaking process is de-phosphorization, and high dephosphorization ability and reasonable melting point are indispensable properties of steelmaking slag. However, phosphate-enriched phases in steelmaking slags hinder its recovery and utilization since phosphorus may reverse to the hot metal [3]. In order to treat and reuse the accumulated steelmaking slag in an environmentally friendly way, various technologies have been developed, such as flotation [4], magnetic separation [5], supergravity separation [6-8], reduction [9-11], and a three-stage continuous selective process (selective enrichment-selective growth-selective

separation) [12-14], to extract phosphate from steelmaking slag. The above-mentioned technologies provide, to some degree, a better understanding of the phosphorus-containing phase formation and its removal from steelmaking slag, and the three-stage continuous selective process is regarded as the most promising process due to its high efficiency and low waste emission. The three-stage-continuous selective process to extract phosphate from steelmaking slag involves the following steps: (1) optimizing the chemical composition of molten slag to promote the enrichment of the targeted phosphorus-rich phase; (2) controlling temperature to promote the crystallization and growth of the phosphorus-rich particles; (3) separating the phosphorus-rich phases from slag according to the difference in physical and chemical properties between phosphorus-rich particles and slag residuals, such as density and magnetic field strength. Of the three steps, the first step is key since it determines the quality of the phosphorus-rich phases and the complexity of subsequent technical steps. Various additives have been applied for optimizing molten slag chemistry to facilitate the generation of phosphorus-rich phases, as summarized in **Table I** [15-22]. Although phosphorus-rich phases were obtained by these processes, the $P_2O_5$ content in the phosphorus-rich phases was less than 20%, particularly for the slag with basicity ($CaO/SiO_2$) above 2.0 [15,23]. Furthermore, the above-mentioned processes require a large amount of additives and significant energy consumption. It is therefore necessary to explore a more efficient additive to modify the steelmaking slag to obtain the phosphorus-richer phase, for example, calcium phosphate ($Ca_{10}P_6O_{25}$). It is well known that $B_2O_3$ addition greatly affects the liquidus temperature [24,25], surface tension [26], fluidity [27], viscosity [27-29], structure [30-32] and crystallization behaviors [33,34] of common metallurgical slags, including blast furnace slag, steelmaking slag, mold slag, etc. Because of its acidic nature, $B_2O_3$ can be used to modify steelmaking slag by reacting with CaO to generate

64 $Ca_2B_2O_5$. Therefore, it can be reasonably expected that a small amount of $B_2O_3$ addition can
65 influence the physicochemical property of steelmaking slag and restrict the precipitation of $nC_2S$-
66 $C_3P$ solid solution to obtain the phosphorus-rich phase (calcium phosphate) efficiently. Furthermore,
67 it has been verified by many investigations [35-37] that the oxidation state of iron depends on oxygen
68 partial pressure, and it is meaningful to obtain the magnetite ($Fe_3O_4$) phase for the purpose of
69 recovering iron resource from steelmaking slag by magnetic separation.

70 In this study, a method is explored to simultaneously recover iron and phosphorus from CaO-
71 $SiO_2$-FeO-$P_2O_5$ slag by oxygen partial pressure control and $B_2O_3$ addition. FactSage 8.1 calculations
72 and confocal laser scanning microscope (CLSM) are employed to predict the precipitated phases
73 and to in-situ observe the crystallization behavior of slags respectively. The reaction mechanisms of
74 molten slag modification by oxygen partial pressure control and $B_2O_3$ addition are discussed.

75 **2. Material and method**

76 **2.1 Materials and Sample Preparation**

77 The chemical composition of synthetic slags is presented in **Table II** and the $P_2O_5$ content in all
78 slags is 10%. The chemical reagents of CaO and $SiO_2$ were dried at 1000 ℃ for 4 hours under Ar
79 atmosphere to remove the small amount of volatiles and hydrones. The synthetic slags were made in
80 a platinum crucible by heating the mixtures of chemical reagents of CaO, $SiO_2$, FeO, $P_2O_5$ and $B_2O_3$
81 at 1600 ℃ in a vertical tube furnace for 2 hours under high purity Ar atmosphere (with flow rate 0.5
82 L/min, 99.999%), and then the slag samples were rapidly quenched into water. Finally, the
83 quenched slag sample was ground for the experiment.

84 **2.2 Experimental Apparatus and Procedure**

85 In this study, the crystallization event was observed in-situ under the CLSM (SVF-SP; Yonekura

MFG. Co. LTD, Japan), and recorded at various temperatures in an Ar atmosphere ($P_{O2}=10^{-6}$ atm). The schematic diagram of the equipment is shown in **Figure 1**.

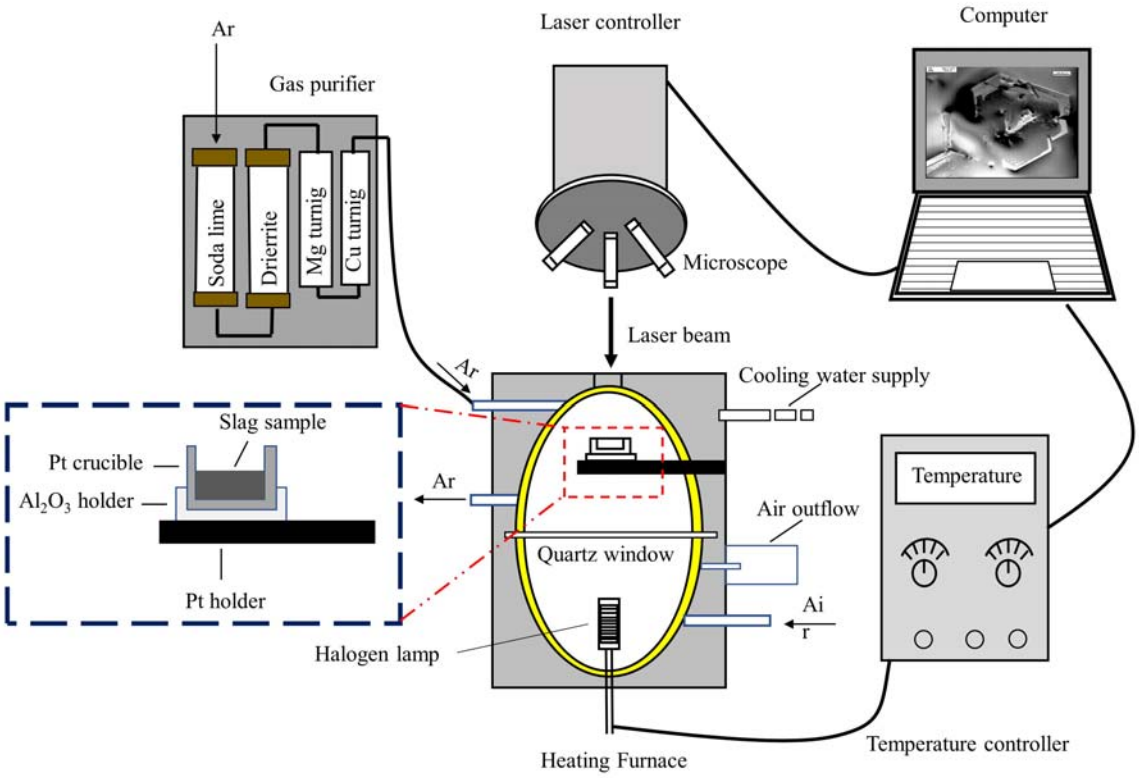


Figure 1 Schematic diagram of CLSM equipment

Prior to each experiment, 0.2 g of the prepared slag was placed in a Pt crucible, heated in the hot stage of CLSM, and held for full melting at 1600 ℃ under Ar gas ($P_{O2}=10^{-6}$ atm) for 5 minutes. Then the molten slag sample was quenched at a cooling rate of 10 ℃/min. The microstructure and elemental distribution of the quenched slag were analyzed through scanning electron microscopy (ZEISS EVO 18) equipped with energy-dispersive X-ray spectroscopy (Xmax50 from Oxford Instrument) (SEM-EDS). Considering that the quantity of quenched slags obtained in the CLSM experiment could not meet the requirement of XRD analysis, repeated experiments were carried out in a vertical tube furnace with 40 g slag in each test to detect the precipitated phases of quenched

samples by XRD (TTRIII from Rigaku Corporation). Complementary SEM-EDS analysis for the samples obtained in the vertical tube furnace was also carried out to verify the results from the samples obtained in the CLSM experiment.

To investigate the effect of oxygen partial pressure on the phase chemistry in the CaO-$SiO_2$-FeO-$P_2O_5$ melt, an experiment was carried out in parallel throughout under air atmosphere ($P_{O2}$=0.21 atm), that is, the molten slag was melted, held and quenched under air. The sample obtained in the experiment under air is thereafter labeled as "0#" slag.

## 3. Results

### 3.1. Thermodynamic Simulation of Precipitated Phases

To investigate the effect of oxygen partial pressure and $B_2O_3$ addition on the crystallization behavior of slags, FactSage 8.1 calculations were conducted to predict the precipitated phases of the slags studied. The calculations comprise two steps of molten slag equilibration and solidification in air ($P_{O2}$=0.21 atm) or Ar ($P_{O2}=10^{-6}$ atm). **Figures 2(a)** and **2(b)** show the change in accumulated amount of different phases precipitated in slags 0# ($P_{O2}$=0.21 atm) and 1# ($P_{O2}=10^{-6}$ atm). The effect of oxygen partial pressure on the precipitation of phosphorus-containing phase ($nC_2S$-$C_3P$) was found negligible. However, it completely changed the iron-containing phase from $Fe_2O_3$ in air ($P_{O2}$=0.21 atm, **Figure 2(a)**) to spinel phase ($Fe_3O_4$) in argon ($P_{O2}=10^{-6}$ atm, **Figure 2(b)**). Similar results were also found in previous papers for exposing the molten CaO-$SiO_2$-FeO-MnO-$Al_2O_3$-MgO slag in Ar atmosphere [38,39].

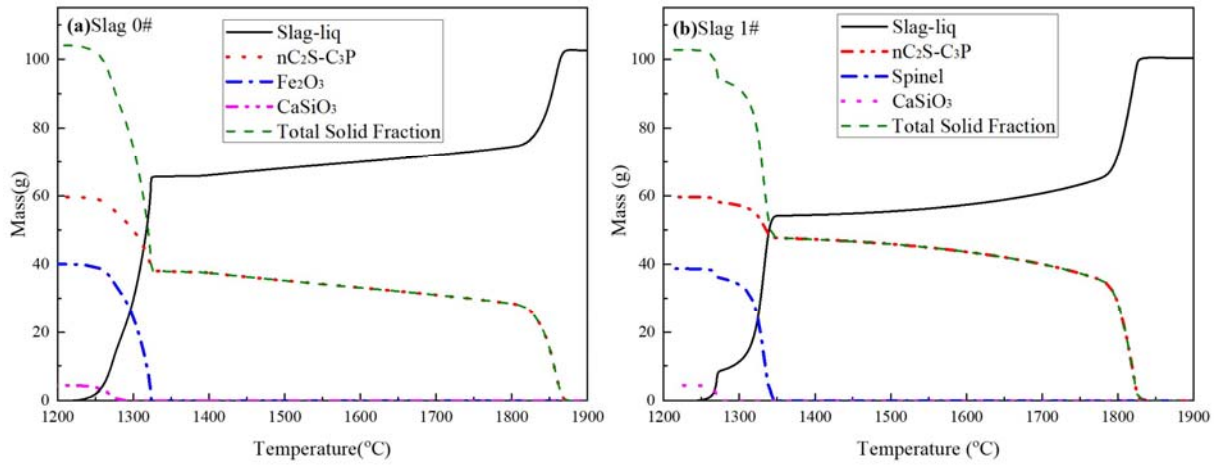


Figure 2 Change in accumulated amount of different phases precipitated from slags with same composition under different oxygen pressures: (a) 0# ($P_{O2}$=0.21 atm); (b) 1# ($P_{O2}$=$10^{-6}$ atm)

**Figures 3(a) to 3(d)** show the change in accumulated amount of different phases precipitated in slags 2#-5# in argon atmosphere ($P_{O2}$=$10^{-6}$ atm) as a function of $B_2O_3$ addition. It was found that with the addition of $B_2O_3$, the primary phase changed from solid solution ($nC_2S$-$C_3P$) phase in slags 2# and 3# to spinel phase ($Fe_3O_4$) in slags 4# and 5#, and phosphorus-containing phases transformed from solid solution ($nC_2S$-$C_3P$) phase in slags 2# and 3# into $Ca_3P_2O_8$ in slags 4# and 5#. As can be seen, the temperature for the precipitation of primary phase and the liquidus temperature, decreased with $B_2O_3$ addition from 2% to 8%. For example, primary phase precipitation occurred at 1706 ℃ (slag 2# - 2% $B_2O_3$), 1544 ℃ (slag 3# - 4% $B_2O_3$), 1311 ℃ (slag 4# - 6% $B_2O_3$) and 1307 ℃ (slag 5# - 8% $B_2O_3$) respectively. The reasons could be attributed to the fact that $B_2O_3$ works as a network former in the molten slag. It absorbs $O^{2-}$ to form [$BO_3$] triangles or [$BO_4$] tetrahedral structural units, thus increasing the amount of network formers and the polymerization degree of the slag. Therefore, the diffusion of slag components in the slag is retarded, which is unfavorable to the precipitation of crystalline phases, leading to the weakening of slag melt crystallization [40,41]. It is interesting to note that with increasing $B_2O_3$ content from 2% (slag 2#) to 8% (slag 5#), the amount of precipitated spinel ($Fe_3O_4$) decreases slightly from 32.7 g to 27.0 g, while that of $Ca_3Fe_2Si_3O_{12}$ increases from 19.6 g to 38.7g. This will be discussed in the section “3.3 Phase Characterization”.

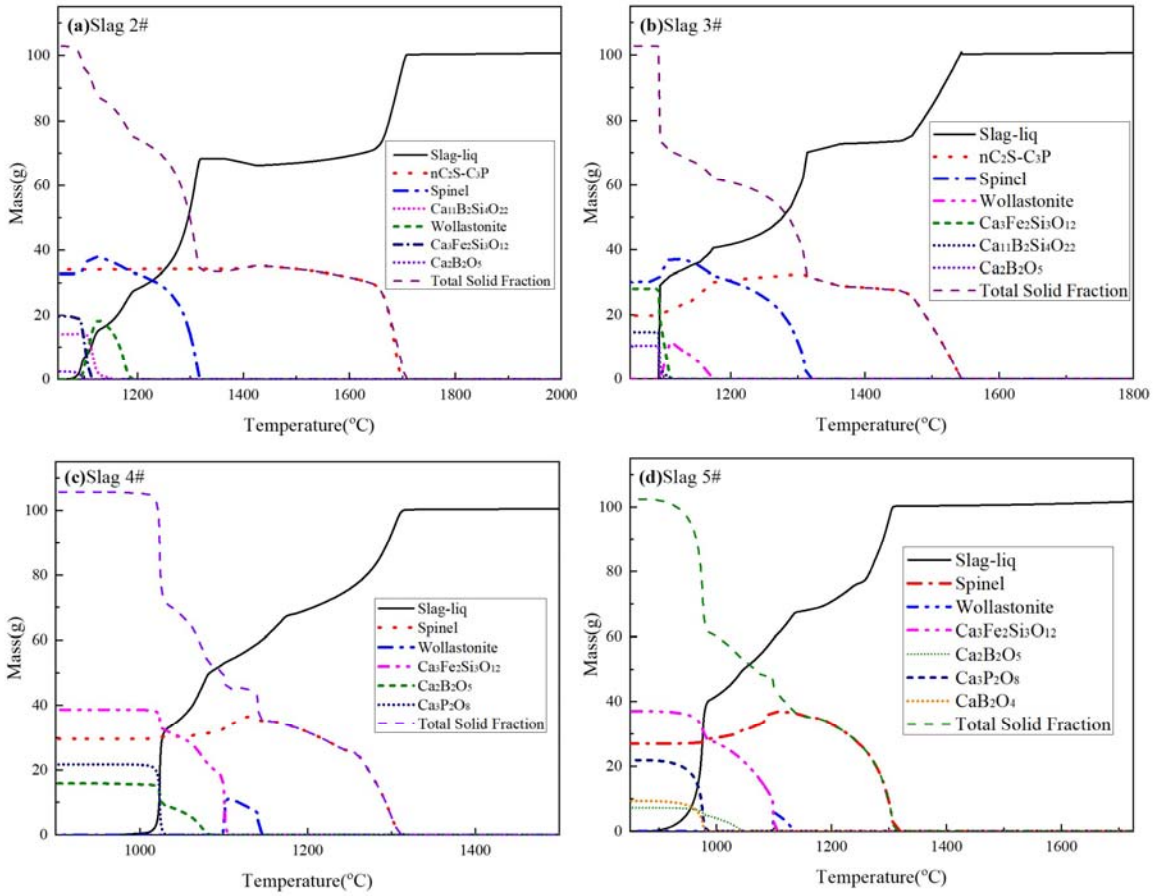


Figure 3 Change in accumulated amount of different phases precipitated from slags in an Ar atmosphere ($P_{O2}=10^{-6}$ atm) as a function of $B_2O_3$ addition: (a) 2# - 2% $B_2O_3$; (b) 3# - 4% $B_2O_3$; (c) 4# - 6% $B_2O_3$; (d) 5# - 8% $B_2O_3$.

**Figure 4** shows the change in the accumulated amount of (a) $Fe_3O_4$ (spinel) and (b) $Ca_3P_2O_8$ in synthetic slags. With changing oxygen partial pressure from 0.21 (slag 0#) atm to $10^{-6}$ atm (slag 1# to slag 5#), the content of spinel phase increased from 0 g (slag 0#) to 38.67 g (slag 1#) per 100g slag. However, with increasing $B_2O_3$ addition from 2% (slag 2#) to 8% (slag 5#), the content of spinel phase ($Fe_3O_4$) gradually decreased from 32.71g to 26.98 g per 100g slag. As can be seen in **Figure 3** and **Figure 4(b)**, $Ca_3P_2O_8$ does not exist in slag 2# (2% $B_2O_3$) and slag 3# (4% $B_2O_3$), but reaches 21.85 g in slag 4# (6% $B_2O_3$) and remains almost unchanged in slag 5# (8% $B_2O_3$), indicating that $Ca_3P_2O_8$ is saturated in the slag with 6% $B_2O_3$.

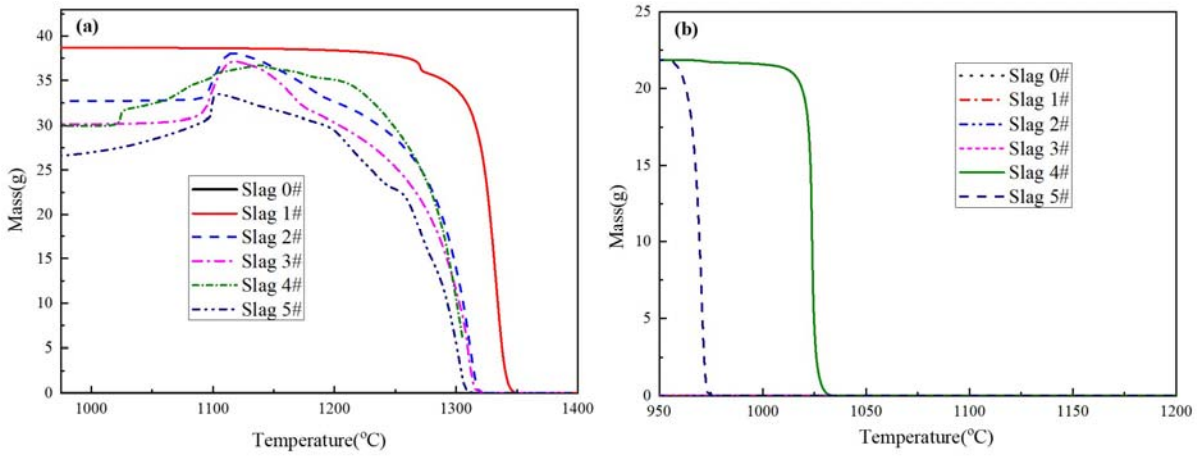


Figure 4 Change in the accumulated amount of (a) $Fe_3O_4$ and (b) $Ca_3P_2O_8$ precipitated from different slags

### 3.2 Crystallization Behaviors of the Slags with varying $B_2O_3$ additions

**Figure 5** shows the crystallization behaviors of the synthetic slag 4# (6% $B_2O_3$) in argon ($P_{O2}=10^{-6}$ atm) observed under CLSM at the cooling rate of 10 ℃/min. For example, the morphology of the pre-melted slag at 1600 ℃ (**Figures 5(a)**), the nucleus of the 1st phase crystal (C1) formed at 1243 ℃ (**Figure 5(b)**), and the frame of crystal formed at ~1216 ℃ (**Figure 5(c)**). With decreasing the temperature from 1243 ℃ to 1082 ℃, the volume of the crystal nucleus increased gradually (**Figures 5(b)-5(e)**). It is noticeable that the frame of the 2nd phase crystal (C2) formed at ~1082 ℃ in **Figure 5(e)** and both phase crystals continuously grew in the temperature ranges from 1082 ℃ to 917 ℃. Finally, the liquid slag appeared to have fully crystallized at 917℃ in **Figure 5(h)**.

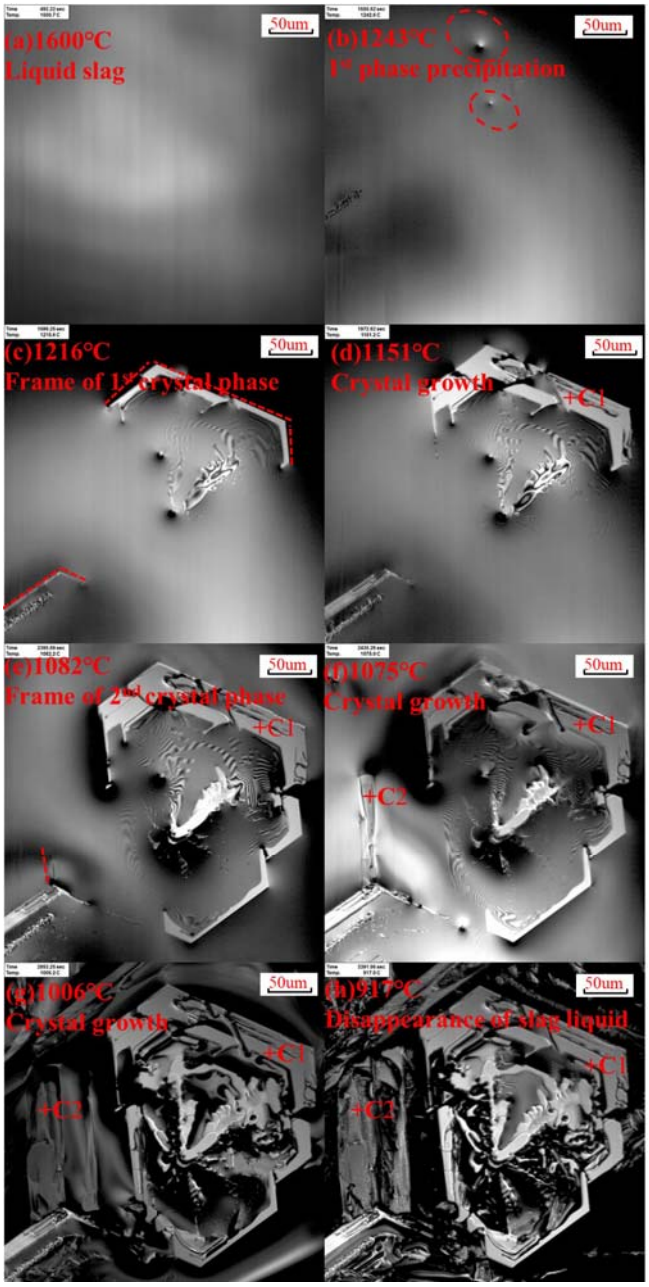


Figure 5 Crystallization process of slag 4# in argon ($P_{O2}$=$10^{-6}$ atm) at the continuous cooling rate of 10 ℃/min: (a) 1600 ℃; (b) 1243 ℃; (c) 1216 ℃, (d) 1151 ℃; (e) 1082 ℃; (f) 1075 ℃; (g) 1006 ℃; and (h) 917 ℃

**Figure 6** compares the CLSM morphology of the crystalline in the slag 4# at the continuous cooling rate of 10 $^{o}$C/min with the corresponding SEM morphology, indicating good agreement between these two. As shown in **Figure 6(b)**, mainly three phases in the slag 4# were observed, namely the lath-shaped phase (P1 and P2), white hexagonally faceted crystal (P3 and P4) and slag

matrix (P5 and P6). It is noticeable that these white hexagonally faceted crystals were surrounded by the lath-shaped phase and slag matrix, indicating an early crystallization, in comparison to the lath-shaped phase and slag matrix. Moreover, the length of lath-shaped crystals was no more than 500 μm, while the diameter of these white crystals was approximately 200 μm. In order to determine the elementary distribution in different phases, EDS mapping analysis was employed and the corresponding results were presented in **Figure 7**. Phosphorus was mainly enriched in the lath-shaped phase, while Fe was mainly concentrated in the white hexagonally faceted phase. Moreover, Ca and Si were concentrated in the matrix phase. EDS spot analysis (**Table** III) indicated that the lath-shaped phase was close to $Ca_2PO_{4.8}$ (or $Ca_2PO_4$), while the white hexagonally faceted phase and slag matrix were approaching $Fe_3O_{3.9}$ (or $Fe_3O_{4.2}$) and $CaFe_{0.3}Si_{0.7}O_{2.1}$ (or $CaFe_{0.3}Si_{0.8}O_{2.1}$) respectively.

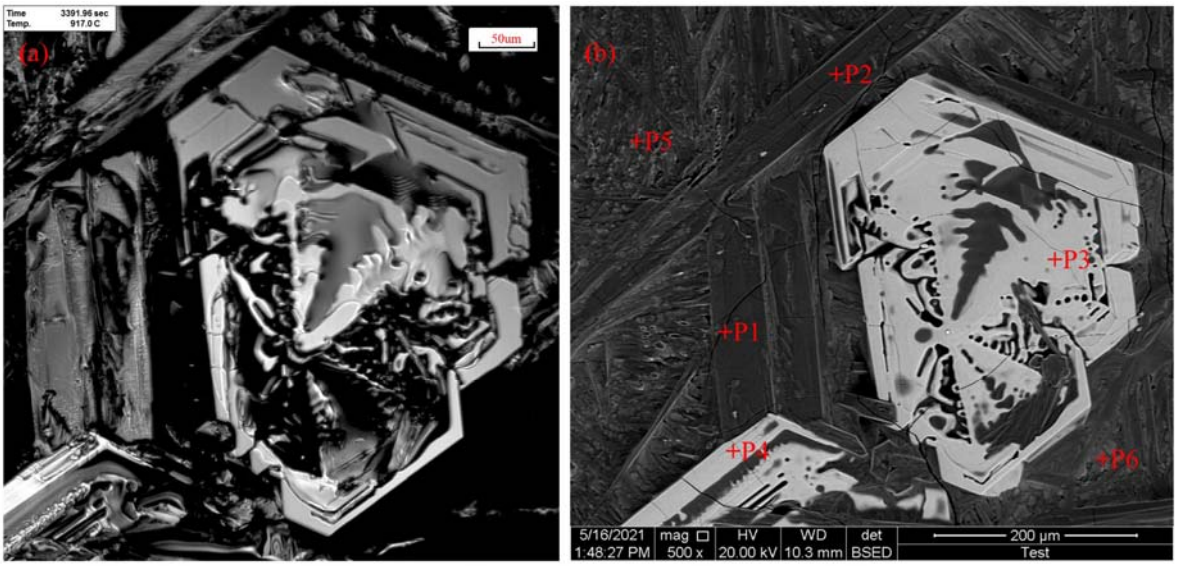


Figure 6 Morphologies of the crystalline in the slag 4# at the continuous cooling rate of 10 °C/min (a) CLSM image and (b) SEM image

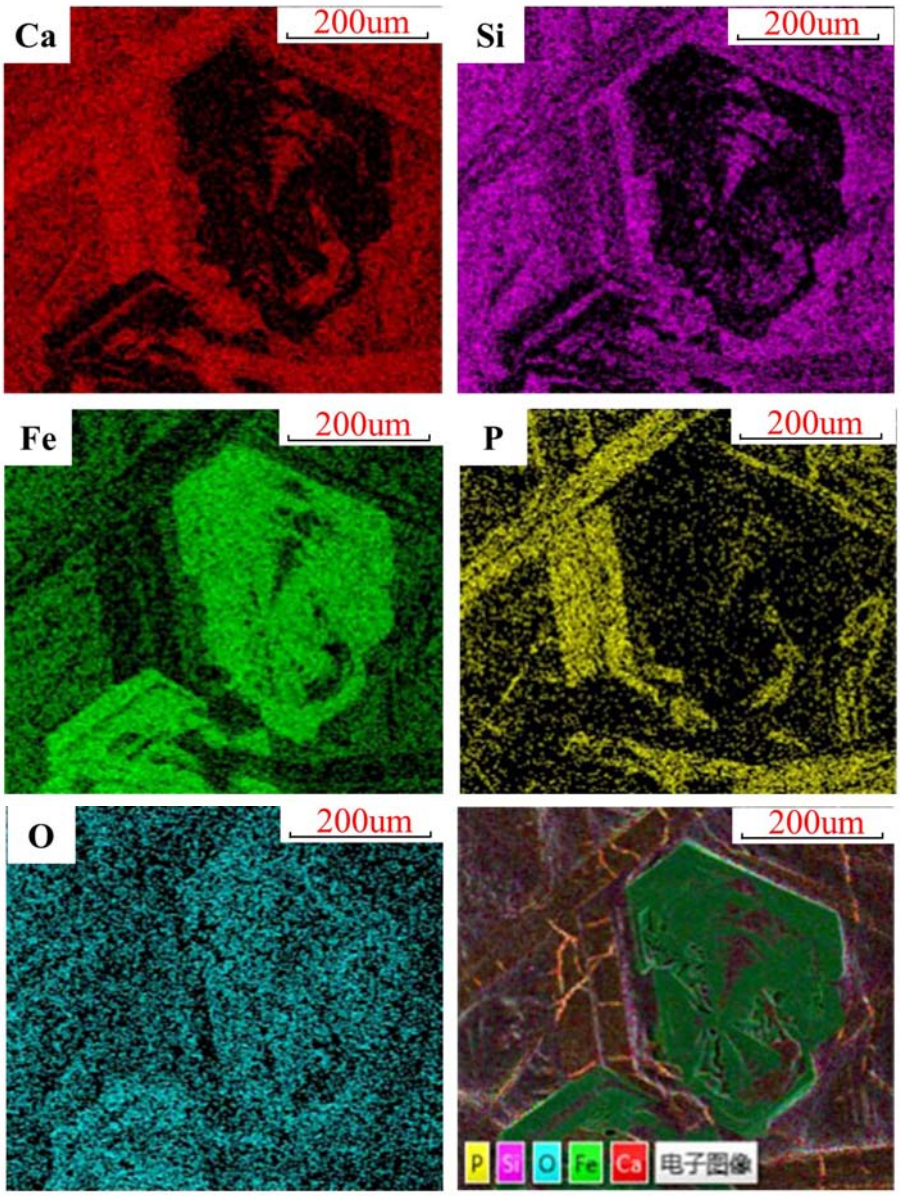


Figure 7 EDS map scanning of slag 4# at the continuous cooling rate of 10 ℃/min

The crystallization behaviors observed by CLSM and precipitated phases analyzed by XRD and SEM-EDS were similar for other slags but not reproduced here for the brevity of the paper. However, the comparison of precipitated phases for slag 1# (without $B_2O_3$ addition) and slag 4# (6% $B_2O_3$) was summarized in **Table IV**. As shown in **Table IV**, a lath-shaped morphology as the 1st precipitated phase and a hexagonally faceted crystal as the 2nd precipitated phase for the slag 1# were observed to start precipitating at 1301 ℃ and 1264 ℃ respectively, while it was the inverse of

192 phase precipitation sequence for the slag 4#. Moreover, the potential formula of the hexagonally
193 faceted phases for both slag 1# and slag 4# was close to magnetite phase ($Fe_3O_4$), while the lath-
194 shaped phase was close to $Ca_7Si_{3.6}P_{2.5}O_{12}$ (or $Ca_7Si_{3.9}P_{2.4}O_{10.3}$) for slag 1# and $Ca_2PO_{4.8}$ (or $Ca_2PO_4$)
195 for slag 4# respectively. The different phase precipitation sequence and potential formula of the
196 precipitated phases for slags 1# and 4# could be attributed to factors such as undercooling [42], slag
197 composition [43] and enthalpy of mixing (so-called Jackson α factor) [44]), which will be reported in a
198 separate paper.

199 **3.3 Phase Characterization**

200 In order to explore the effect of oxygen partial pressure and $B_2O_3$ addition on the crystallization
201 process of samples, the phases presented in the slags were characterized using XRD. **Figures 8(a)**
202 to **8(f)** show phases presented in the slag 0# to 5# at the continuous cooling rate of 10 °C/min. It
203 should be pointed out that slag 0# was cooled in air ($P_{O2}$=0.21 atm), while slags 1# to #5 were
204 cooled in argon atmosphere ($P_{O2}=10^{-6}$ atm). As can be seen in **Figure 8(a)**, it was shown clearly that
205 three phases were detected in slag 0#, namely $Ca_2Fe_2O_5$, $Ca_7Si_2P_2O_{16}$ and $Ca_2SiO_4$. Fe existed in the
206 form of calcium ferrite phase, while P was concentrated in the $Ca_7Si_2P_2O_{16}$ phase in the synthetic
207 slag 0# ($P_{O2}$=0.21 atm). However, with changing oxygen partial pressure from 0.21 atm (slag 0#) to
208 $10^{-6}$ atm (slag 1#), the predominant iron-containing phase ($Ca_2Fe_2O_5$) transformed into magnetite
209 phase ($Fe_3O_4$), as shown in **Figure 8(b)**, while other phases remained the same as in the slag 0#.
210 Compared with slag 1#, dicalcium silicate ($Ca_2SiO_4$) was not detected in slag 2#, while two new
211 phases of $CaFeSi_2O_6$ and $Ca_{11}B_2Si_4O_{22}$ were found after adding 2% $B_2O_3$ as shown in **Figure 8(c)**.
212 As can be seen in **Figure 8(d)** for slag 3# containing 4% $B_2O_3$, the phosphorus-rich phase of
213 calcium phosphate ($Ca_{10}P_6O_{25}$) was detected and the B-containing phase was identified as the

calcium borate phase ($Ca_2B_2O_5$), rather than $Ca_{11}B_2Si_4O_{22}$. As for the slags with $B_2O_3$ addition of 6% (slag 4#) and 8% (slag 5#), calcium phosphate ($Ca_{10}P_6O_{25}$) remained the only phosphorus-rich phase, and the B-containing phase transformed from $Ca_2B_2O_5$ (Slag #3) to $CaB_2O_4$ (Slags 4# and 5#). In summary, with simultaneous change of oxygen partial pressure from 0.21 atm (in air) to $10^{-6}$ atm (in argon) and addition of $B_2O_3$ (6%) into the simulated steelmaking slag, phosphorus- and iron-containing phases precipitated in the form of $Fe_3O_4$ and $Ca_{10}P_6O_{25}$ respectively during the cooling process from 1600 $^{o}$C to 900 $^{o}$C.

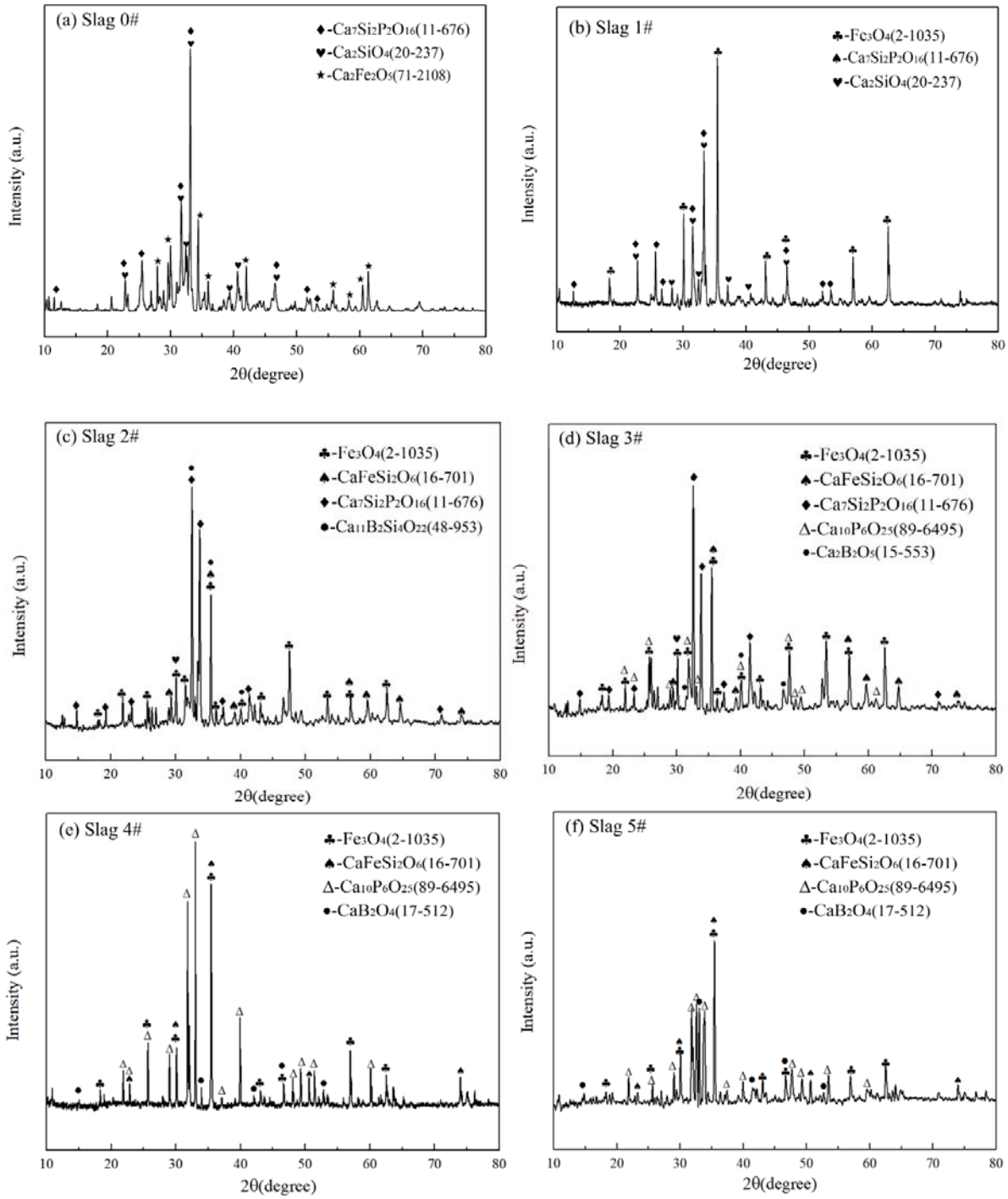


Figure 8 X-ray diffraction patterns of samples at the continuous cooling rate of 10 ℃/min: (a) Slag 0#; (b) Slag 1#; (c) Slag 2#; (d) Slag 3#; (e) Slag 4#; (f) Slag 5#

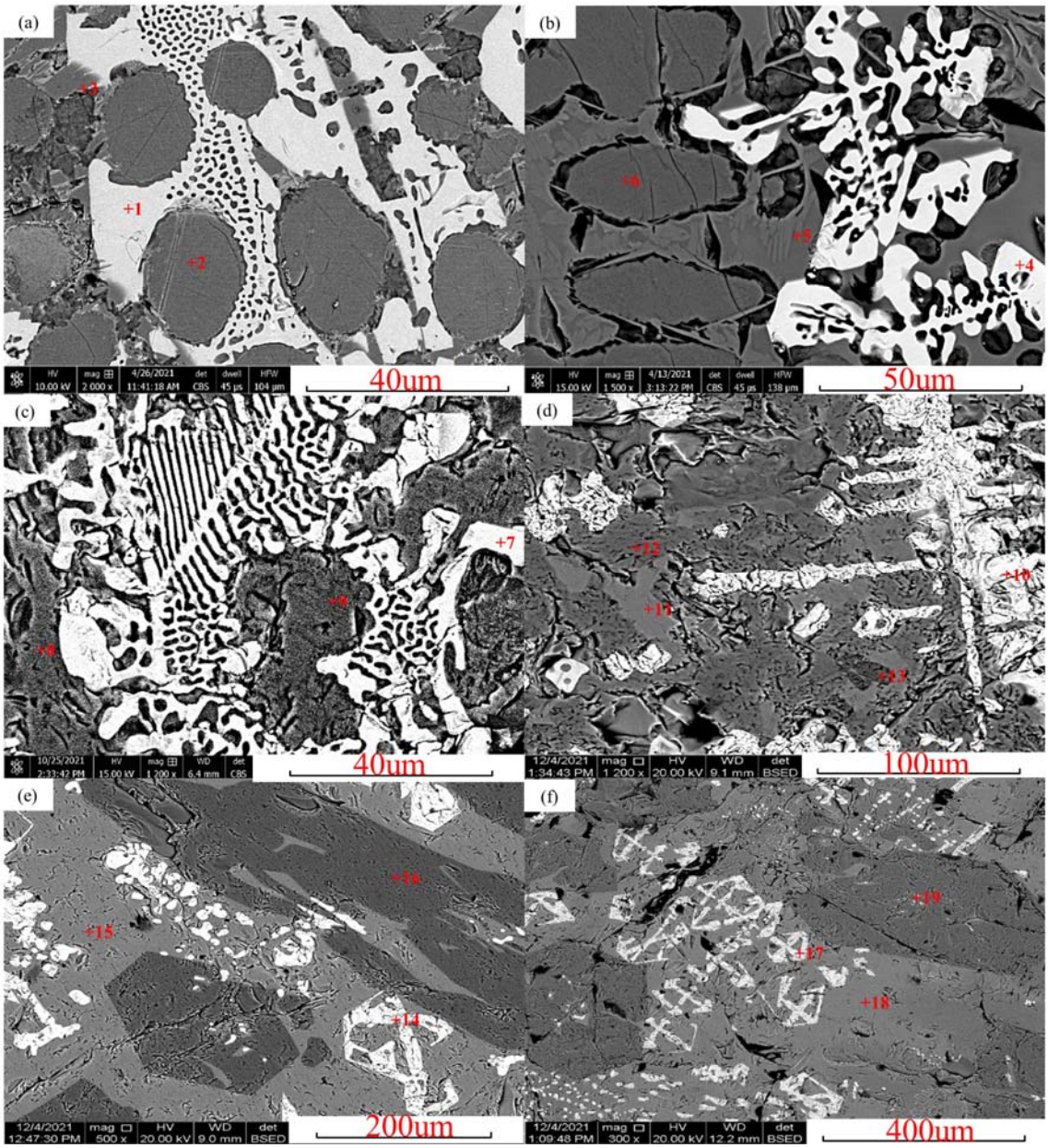


Figure 9 SEM results of six samples: (a) Slag 0#; (b) Slag 1#; (c) Slag 2#; (d) Slag 3#; (e) Slag 4#; (f) Slag 5#. Slag 0# was cooled in air ($P_{O2}$=0.21 atm) while slags 1# to 5# were cooled in argon ($P_{O2}=10^{-6}$ atm).

From SEM-EDS analysis (**Figure 9** and **Table V**), it is clear that the irregular white phase in **Figure 9(a)** is composed primarily of Ca, Fe and O, while the spinel type and/or dendritic white phases in **Figures 9(b)-9(f)** are made up of Fe and O, with chemical formula approaching $Fe_3O_4$. It indicates that oxygen partial pressure is the key to the transformation of iron oxides in the CaO-$SiO_2$-FeO-$P_2O_5$ slags. In **Figures 9(a)-9(b)**, the round granular phase was primarily made up of Ca,

234 Si, P and O, corresponding to the phosphate-containing phase of $Ca_7Si_2P_2O_{16}$, while the slag matrix
235 was composed primarily of Ca, Si and O, corresponding to the dicalcium silicate ($2CaO \cdot SiO_2$). As
236 can be seen from **Figures 9(c)-9(f)**, the dark lath-shaped or/and faceted morphology phase started to
237 form in slag 3# (4% $B_2O_3$, **Figure 9(d)**) and enlarged with increasing $B_2O_3$ content, which could be
238 attributed to the fact that $B_2O_3$ addition gave rise to a decrease in slag viscosity. As Ca, P and O
239 were enriched in the abovementioned dark phase and the chemical formula was close to the
240 phosphorus-rich phase of calcium phosphate ($Ca_{10}P_6O_{25}$), it is reasonable to conclude that $B_2O_3$ is
241 an effective additive to extract phosphate from steelmaking slag.

242 By comparing the integrated intensities of the diffraction peaks from each of the known phases,
243 the weight fractions of phosphorus- and iron-containing phases in the slags were semi-quantitatively
244 determined and listed in **Table VI**. As seen in **Table VI**, by changing the oxygen partial pressure
245 from 0.21 atm (slag 0#) to $10^{-6}$ atm (slag 1#), the amount of magnetic phase greatly increased from
246 0 g to 38 g while that of the solid-solution phase ($Ca_7Si_2P_2O_{16}$) varied slightly. With $B_2O_3$ addition
247 from 2% (slag 2#) to 8% (slag 5#), the amount of solid-solution ($Ca_7Si_2P_2O_{16}$) phase in argon
248 ($P_{O2}=10^{-6}$ atm) decreased from 29 g to 0 g, while that of calcium phosphate ($Ca_{10}P_6O_{25}$) first
249 increased and then decreased, with the maximum of 28 g per 100 g slag at 6% $B_2O_3$ addition (slag
250 4#). Moreover, the quantity of spinel ($Fe_3O_4$) decreases slightly while that of $CaFeSi_2O_6$ increases
251 with increasing $B_2O_3$ content, which agree well with the results of thermodynamic calculation in
252 this paper. The reasons could be attributed to the fact that high melting point substances could be
253 transformed into low melting point phases by adding $B_2O_3$ into slags [45-47]. In this case, it could be
254 deduced that a small amount of low melting point phase of $CaFeSi_2O_6$ (1217℃) was generated
255 through the reaction (1).

$$CaO + FeO + 2SiO_2 = CaFeSi_2O_6 \quad (1)$$

$$\Delta G = -121874.7 + 21.11T\,[J/mol]$$

By combining the crystallization behavior observed by CLSM, the microstructure analyzed by SEM-EDS and the phases present in the slags characterized by XRD, for the slag 1#, the 1st and 2nd phases observed at 1301 ℃ and ~1264℃ can be considered solid-solution ($Ca_7Si_2P_2O_{16}$) and magnetite ($Fe_3O_4$). This agrees with the calculation result by FactSage 8.1 (**Figure 2(b)**). Similarly, it could be concluded that the 1st and 2nd phases in slag 4# observed at 1243 ℃ in **Figure 5(b)** and ~1082 ℃ in **Figure 5(e)** are $Fe_3O_4$ and $Ca_{10}P_6O_{25}$ respectively.

## 4. Discussion

### 4.1 Influence of Oxygen Partial Pressure

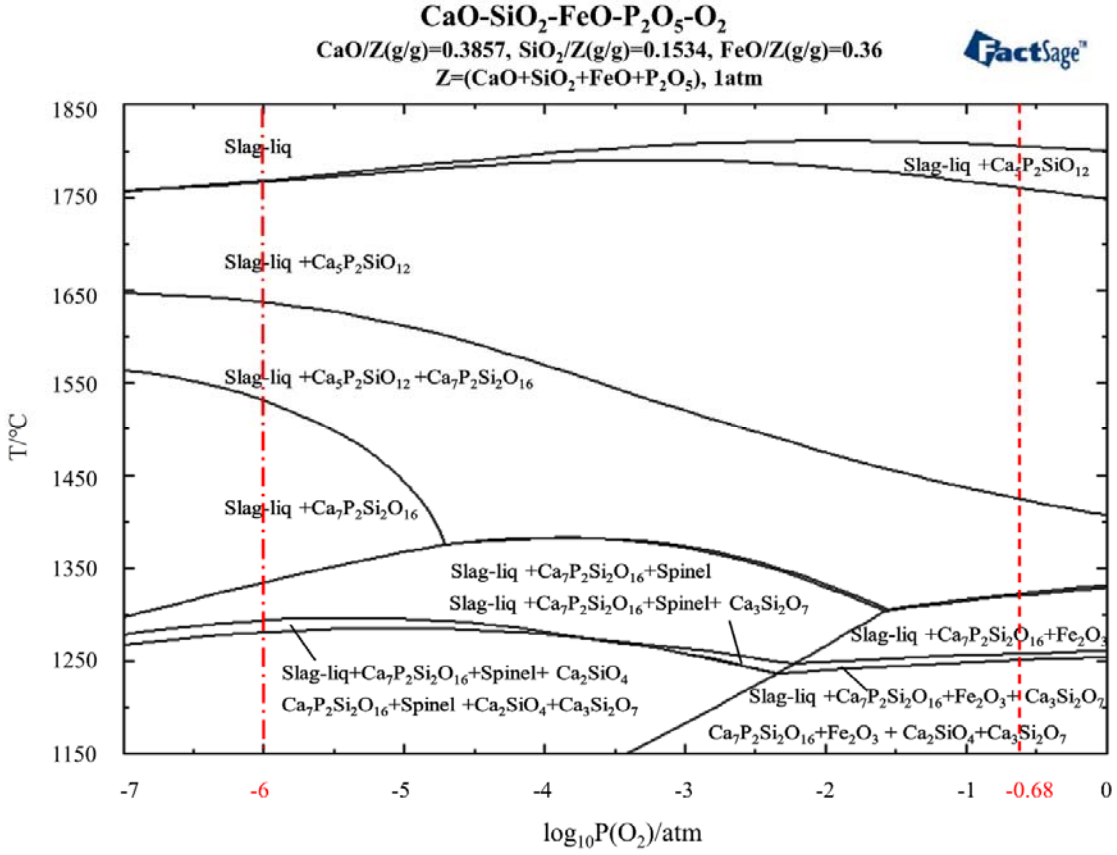


Figure 10 Phase diagram of $CaO\text{-}SiO_2\text{-}FeO\text{-}P_2O_5$ system with the dotted line and dot-dash line corresponding to oxygen partial pressure in air and argon respectively.

**Figure 10**, the phase diagram of $CaO-SiO_2-FeO-P_2O_5$ slag, demonstrates that the presence of iron oxide species in the solid product depends on oxygen partial pressure. Wustite (FeO) in the slag is oxidized to magnetite under the oxygen pressure of $10^{-6}$ atm or to hematite under the oxygen pressure of 0.21 atm. It should be pointed out that the precipitated phases of the slag that have been described by the phase diagrams in **Figure 10** are for equilibrium conditions, which can be approximated by slow cooling. However, the relatively large cooling rate of 10 ℃/min is applied in this study, causing the deviation from equilibria between the slag samples and the gas atmosphere. Fortunately, the main precipitated phases, such as magnetite ($Fe_3O_4$), $Ca_7Si_2P_2O_{16}$ and $Ca_2SiO_4$, predicted by phase diagrams in **Figure 10** and characterized by the XRD pattern (in **Figure 8(b)**) keep the same. For industry applications, in order to recover iron from the slag in the form of magnetite ($Fe_3O_4$) by magnetic separation, the molten slag should be solidified at a slow cooling rate from about 1350 ℃ as illustrated in **Figure 10** to give $Fe_3O_4$ enough time to precipitate. In addition, for the air-treated slag (slag 0#), $Fe^{2+}$ in the slag (FeO) is oxidized to $Fe^{3+}$ ($Fe_2O_3$) according to reaction (2) as shown in **Figure 10.** However, the XRD pattern (**Figure 8(a)**) for the air-treated slag (slag 0#) demonstrates the presence of the main iron-containing phase $Ca_2Fe_2O_5$ rather than $Fe_2O_3$, implying that the formed hematite further stabilizes the free lime by forming $Ca_2Fe_2O_5$ according to reaction (3).

$$2FeO + 1/2O_2 = Fe_2O_3 \quad (2)$$

$$2CaO + Fe_2O_3 = Ca_2Fe_2O_5 \quad (3)$$

The deviation of the prediction and experimental result could be attributed to different conditions for the calculations and laboratory experiments, that is, the experimental conditions might be far from the equilibrium state in the thermodynamic prediction. In the actual crystallization process, reactions are affected by various kinetic factors such as the reaction time, the reaction area of the system studied, etc. It is evidenced that the $Ca_2Fe_2O_5$ phase is the dominant iron-containing phase in the steelmaking slag under high oxygen partial pressure (e.g. in the air) [21, 38,39].

In contrast, for the slags treated in Ar atmosphere ($P_{O2}$ = $10^{-6}$ atm), the oxidizing processes in the molten slag can be expressed by reaction (4):

$$6FeO + O_2 = 2Fe_3O_4 \quad (4)$$

As seen in **Figure 8(b)**, spinel ($Fe_3O_4$) is the stable solid iron oxide under Ar atmosphere ($P_{O2}$ = $10^{-6}$ atm) in the present study. This is also supported by the fact that the magnetite ($Fe_3O_4$) primary phase field has replaced the hematite ($Fe_2O_3$) primary phase field as the dominant feature of the iron oxide-rich corner of the CaO-$FeO_x$-$SiO_2$ diagram at the effective oxygen partial pressure between $10^{-3.9}$ and $10^{-3.7}$atm [21].

To summarize, oxygen partial pressure is the key to oxidation state of iron oxides in the CaO-$SiO_2$-FeO-$P_2O_5$ melt. In air, FeO is oxidized to $Fe_2O_3$, which combines with free lime in the slag to form $Ca_2Fe_2O_5$, while under an atmosphere with low oxygen partial pressure, FeO is oxidized to $Fe_3O_4$.

### 4.2 Influence of $B_2O_3$ addition

**Figure 11** shows Gibbs free energy change of relevant reactions as a function of temperature calculated by FactSage 8.1. It clearly shows that the descending order for component formation is $3CaO{\cdot}P_2O_5$ (reaction (5)) > $2CaO{\cdot}B_2O_3$ (reaction (6)) > $2CaO{\cdot}SiO_2$ (reaction (7)). The preferential formation of $2CaO{\cdot}B_2O_3$ rather than $2CaO{\cdot}SiO_2$ inhibits the generation of solid-solution $nCaO{\cdot}SiO_2$-$3CaO{\cdot}P_2O_5$ in the slag. It is in accord with the phase precipitation sequence observed by CLSM in **Figure 5** and the precipitated phases characterized by XRD in **Figure 8**. The reasons could be attributed to not only the activity of CaO in the slag becomes small with the $B_2O_3$ addition based on the thermodynamic calculation and molecular theory for slag structure proposed by H. Schenck [48,49], but also the reaction mechanism in the molten $B_2O_3$ modification process demonstrated by the theory of bond parameter function [50].

It should be pointed out that $B_2O_3$ addition to the molten slag causes two contradictory effects on nucleation and growth of the magnetic spinel phase ($Fe_3O_4$). First, $B_2O_3$ can lower the melting temperature and viscosity of slag by forming a series of low-melting compounds, which is beneficial for the migration of ions and molecules in the molten slag, resulting in the growth of $Fe_3O_4$ crystals. Secondly, $B_2O_3$ addition can also weaken the crystallization ability of $Fe_3O_4$ phase by increased component diffusion resistance originating from the increased polymerization degree of slag melts, resulting in the small nucleation rate of $Fe_3O_4$ phase. In fact, the intensity of characteristic peaks of $Fe_3O_4$ phase slightly decreased with the increase of $B_2O_3$ addition from 2% to 8% as obviously illustrates in **Figures 8c** to **8f**. In view of these two aspects, it seems that $B_2O_3$ plays a little bit antagonism effect on the precipitation of $Fe_3O_4$ phase from the molten synthetic slags under Ar atmosphere.

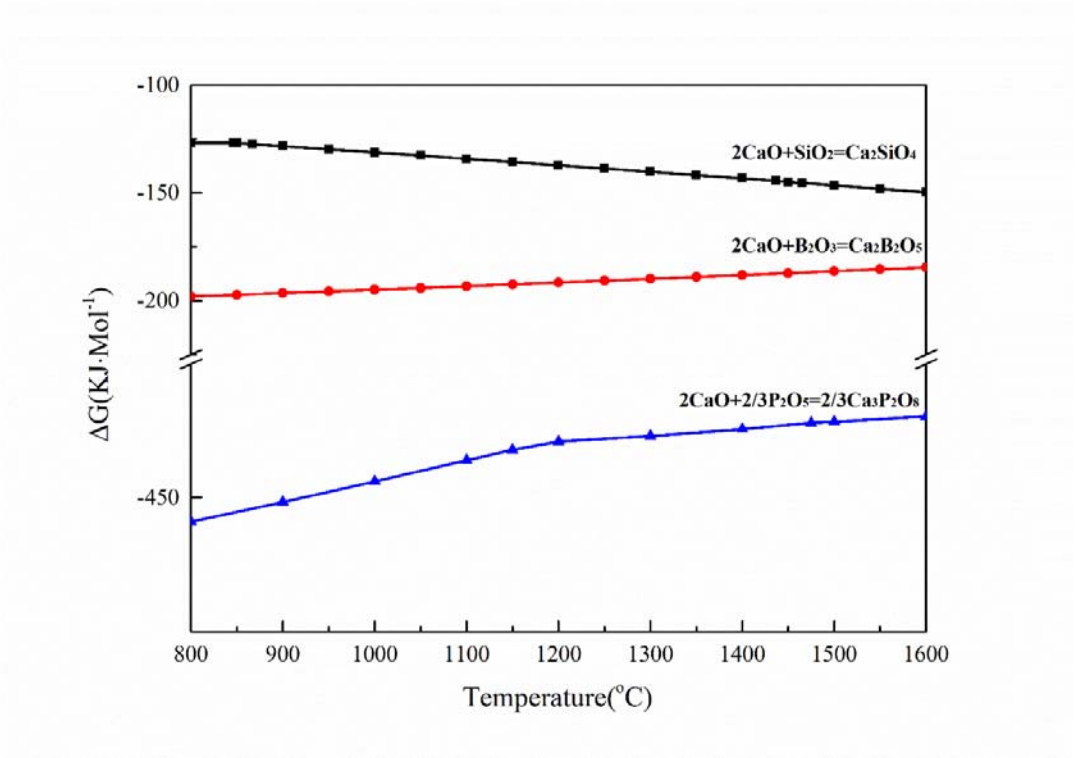


Figure 11 Gibbs free energy change of relevant reactions calculated by FactSage 8.1

Combining the results of thermodynamic calculation, crystallization behavior observed through CLSM, microstructure analyzed by SEM-EDS and the phases present in the slags characterized by XRD, reactions during slag modification with $B_2O_3$ addition can be expressed in Eqs. (5)-(7), and the schematic diagram of the molten slag modification by atmosphere control and $B_2O_3$ addition could be illustrated in **Figure 12.** Compared with the previous processes in **Table I**, the new process has two advantages: the lower energy consumption and smaller amount of additive $B_2O_3$ required. First, $B_2O_3$ was added into molten steelmaking slag during the slag tapping process, and the specific heat capacity for steelmaking slag is about 800 J/(kg·°C) [51-54]. Therefore, the new process uses at least 355 kW h/t sensible heat of molten steelmaking slag and meanwhile avoids at least 290 kW h/t reheating for the modification in previous processes in **Table I**. Second, the $B_2O_3$ amount in the new process is smaller than that in the previous processes in **Table I**.

$$3CaO + P_2O_5 = Ca_3P_2O_8 \quad (5)$$

$$CaO + B_2O_3 = CaB_2O_4 \quad (6)$$

$$2CaO + SiO_2 = Ca_2SiO_4 \quad (7)$$

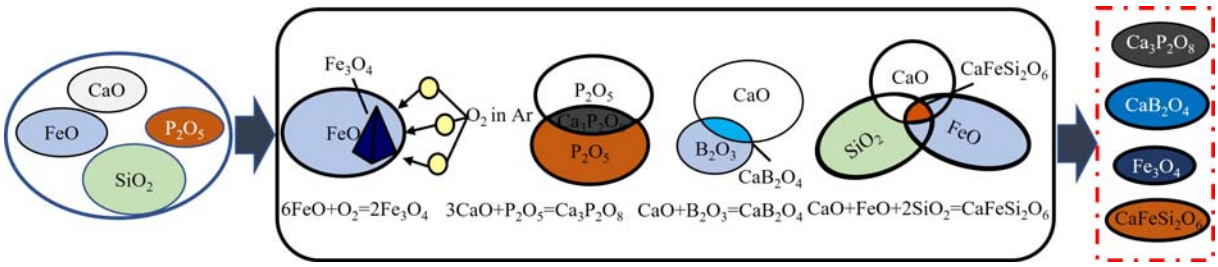


Figure 12 Schematic diagram of the slag modification

The current study confirms that Fe and P in synthetic steelmaking slags can be concentrated in the form of magnetite ($Fe_3O_4$) and calcium phosphate ($Ca_{10}P_6O_{25}$) phases by oxygen partial pressure control and $B_2O_3$ addition. Subsequently, the optimum temperature range for the crystallization of $Fe_3O_4$ and $Ca_{10}P_6O_{25}$ phases was obtained as (1055 ± 25)°C by both theoretical calculation and experiment [55]. In order to separate phosphorus and iron phases from the quenched slags, a wet magnetic separator (XCGQ-500 with the magnetic field intensity of 3.0 KOe was firstly employed to separate magnetite phase from the slag bulk. Subsequently, the flotation machine (XFD-0.75L) was used to separate the phosphorus-enriched phase from the non-magnetic part of magnetic separation. Using a combination of magnetic separation and flotation, the concentrates were obtained with $Fe_3O_4$ and $P_2O_5$ content of 92.84 % and 37.66 % respectively, corresponding to the recovery ratios of 85.8 % for iron and 91.3 % for phosphorus. The recycled materials of iron and phosphorus concentrates could be considered as a potential source for ferrous feedstock and phosphate fertilizer respectively [56].

## 5. Conclusion

In this study, the effect of oxygen partial pressure and $B_2O_3$ addition on the crystallization behavior of iron- and phosphorus-containing phases in a $CaO$-$SiO_2$-$FeO$-$P_2O_5$ melt has been investigated. The main conclusions can be summarized as follows:

(1) Recovery of iron and phosphorus from the $CaO$-$SiO_2$-$FeO$-$P_2O_5$ slag can be effectively achieved through oxygen partial pressure control and $B_2O_3$ addition, through the precipitation in the melt of magnetite ($Fe_3O_4$) and calcium phosphate ($Ca_{10}P_6O_{25}$) phases respectively.

(2) Oxygen partial pressure is the key to the precipitation of iron oxides in the $CaO$-$SiO_2$-$FeO$-$P_2O_5$ slags. Both thermodynamic calculation and experimental results indicated that with decreasing oxygen partial pressure from 0.21 atm to $10^{-6}$ atm, the precipitated iron oxides transformed from ferric oxide ($Fe_2O_3$) to magnetite ($Fe_3O_4$).

(3) Both thermodynamic calculation and experimental result indicated that by adding $B_2O_3$ from 2% to 8%, the amount of calcium phosphate ($Ca_{10}P_6O_{25}$) first increased and then decreased, with the maximum occurring at 6% $B_2O_3$.

**Acknowledgment**

This work was supported by Jiangsu University (19JDG011)，the Project of the National Natural Science Foundation of China (Grant No.51874272 and No. 52111540265) and Open Foundation of State Key Laboratory of Mineral Processing (No. BGRIMM-KJSKL-2022-23). J LI would like to acknowledge the support from innovation training program for undergraduate (202010299076 and 202110299463X) and scientific research projects (18A001, 18A003,18A014 and 20A007).

**Conflict of Interest**

The authors declare no potential conflict of interest.

## Reference


[1] J. F. Li, C. X. Luo, M. K. Sun, W. G. Shen, B. Cao, and X. L. Li. *Key Eng. Mater*, **2014**, vol. 3019, pp. 98-102.

[2] L. Lin, Y. Q. Liu, J. G. Zhi, S. He, X. Li, Z. X. Hou, and L. Q. Zhang. *Ironmak. Steelmak.*, **2021**, vol.48, pp. 334-42.

[3] X. M. Yang, M. Zhang, G. M. Chai, J. Y. Li, Q. Liang, and J. Zhang. *Ironmak. Steelmak.*, **2016**, vol.43, pp. 663-87.

[4] Z. W. Wang, B. Liang, and J. R. Zhang. *Appl. Mech. Mater*, **2014**, vol.3013, pp. 1501-05.

[5] M. Y. Kazuyo, K. Hironari, and N. Tetsuya. *IJSJ Int.*, **2010**, vol.50, pp. 65-70.

[6] X. Lan, J. T. Gao, Y. Du, and Z. C. Guo. *J. Alloys Compd.*, **2018**, vol.731, pp. 873-80.

[7] J. T. Gao, Y. Li, G. L. Xu, F. Q. Wang, Y. Lu, and Z. C. Guo. *ISIJ Int.*, **2017**, vol.57, pp. 587-89.

[8] J. T. Gao, L. Guo, Y. W. Zhong, H. R. Ren, and Z. C. Guo. *Int. J. Miner. Metall. Mater.*, **2016**, vol.23, pp. 743-50.

[9] Y. Y. Zhang, Q.G. Xue, G. Wang, and J. S. Wang. *ISIJ Int.*, **2018**, vol.58, pp. 2219.

[10] M. Sugata, T. Sugiyama, and S. Kondo. *ISIJ Int.*, **1974**, vol.14, pp. 88-95.

[11] S. Takeuchi, N. Sano, and Y. Matsushita. *Tetsu-to-Hagane´*, **1980**, vol.66, pp. 2050-57.

[12] H. M. Xue, J. Li, Y. J. Xia, Y. Wan, L. J. Chen, and C.J. Lv. *Metals*, **2021**, vol.11, pp. 216.

[13] J. M. Gonzalez, C. J. Penn, and S. J. Livingston. *Water*, **2020**, vol.12, pp.1953.

[14] G. F. Ye, J. Yang, R. H. Zhang, W. K. Yang, and H. Sun. *Int. J. Miner. Metall. Mater.*, **2021**, vol.28, pp. 66-75.

[15] J. Y. Li, M. Zhang, M. Guo, and X.M. Yang. *Int. J. Miner. Metall. Mater.*, **2016**, vol.23, pp. 520-33.

405 [16] L. Jiang, J. Diao, X. M Yan, B. Xie, Y. Ren, T Zhang, and G. Z. Fan. *ISIJ Int.*, **2015**, vol.55,
406 pp.564-69.
407 [17] L. Lin, Y. P. Bao, M. Wang, W. Jiang, and H. M. Zhou. *J. Iron Steel Res. Int.*, **2014**, vol.21, pp.
408 496-502.
409 [18] L. Lin, Y. P. Bao, and M. Wang. *ISIJ Int.*, **2014**, vol.54, pp. 2746-53.
410 [19] K. Yu, Y. L. Zhang, F.S. Li, and M. Gao. *J. Iron Steel Res. Int.*, **2018**, vol.26, pp. 796-805.
411 [20] G. Q. Li, C. Y. Zhu, Y. J. Li, X. Y. Huang, and M. Chen. *Steel Res. Int.*, **2013**, vol.84, pp. 687-
412 94.
413 [21] G. J. Chen, and S. P. He. *Ironmak. Steelmak.*, **2014**, vol.42, pp. 433-38.
414 [22] Y. L. Zhang, M. Guo, F.S. Li, and Y. Ke. *Arch. Metall. Mater*, **2018**, vol.63, pp. 1769-83.
415 [23] J. Y. Li, M. Zhang, M. Guo, and X. M. Yang. *Metall. Mater. Trans. B*, **2014**, vol.45, pp. 1666-
416 82.
417 [24] J. Ma, W. Li, G.Q. Fu, and M. Y. Zhu. *J. Sustain. Metall*, **2021**, vol.7, pp. 1190-99.
418 [25] H. M. Wang, T. W. Zhang, H. Zhu, G. R. Li, Y. Q. Yan, and J. H. Wang. *ISIJ Int.*, **2011**, vol.51,
419 pp. 702-06.
420 [26] M. Nakamoto, T. Tanaka, L. Holappa, and M. Hämäläinen. *ISIJ Int.*, **2007**, vol.47, pp. 211-16.
421 [27] S. Ren, J. L. Zhang, L. S. Wu, W. J. Liu, Y. N. Bai, X. D. Xing, and D. W. Kong. *ISIJ Int.,*
422 **2012**, vol.52, pp. 984-91.
423 [28] Y. Shi, Y. G. Wei, S. W. Zhou, B. Li, Y. D. Yang, and H. Wang. *J. Alloys Compd.*, **2020**,
424 vol.822, pp. 153478.
425 [29] A. A. Babenko, R. R. Shartdinov, A. G. Upolovnikova, A. N. Smetannikov, and V. S.
426 Gulyakov. *Izvestiya VUZ.Chernaya Metallurgiya,* **2019***,* vol.62, pp. 769-73.

[30] P. Zhang, J.H. Liu, Z. Wang, G. Qian, and W. Ma. *Metall Mater Trans B,* **2019**, vol.50, pp. 304-11.

[31] J. Qi, C. Liu, and M. Jiang. *ISIJ Int.*, **2018**, vol.58, pp. 186-93.

[32] Y. Sun, J. Liao, K. Zheng, X. D. Wang, and Z. T. Zhang. *JOM*, **2014**, vol.66, pp. 2168-75.

[33] W. L. Wang, J. Y. Chen, J. Yu, L. J. Zhou, S. F. Dai, and W. G. Tian. *Waste Management*, **2020**, vol.111, pp. 34-40.

[34] L. J. Zhou, W.L. Wang, B. X. Lu, G. H. Wen, and J. Yang. *Met Mater Int*, **2015**, vol.21, pp. 126-33.

[35] H. Matsuura, M. Kurashige, M. Naka, and F. Tsukihashi. *ISIJ Int.,* **2018**, vol.49, pp. 1283-89.

[36] S. Y. Cheng, M. Shevchenko, P. C. Hayes, and E. Jak. *Metall Mater Trans B*, **2021**, vol.52, pp. 1891-1914.

[37] J. Chen, M. Shevchenko, P. C. Hayes, and E. Jak. *ISIJ Int.,* **2019**, vol.59, pp. 805-09.

[38] J. C. Li, D. Bhattacharjee, X. J. Hu, D. W. Zhang, S. Sridhar, and Z. S. Li. *Metall Mater Trans B*, **2019**, vol.50. pp. 1931-48.

[39] J .C. Li, D. Bhattacharjee, X. J. Hu, D. W. Zhang, S. Sridhar, and Z. S. Li. *Metall Mater Trans B*, **2019**, vol.50, pp. 1023-34.

[40] Y. Huang, C. B. Shi, X. X. Wan, J. L. Li, D. L. Zheng, and J. Li. *J. Iron Steel Res. Int*, **2021**, pp. 1-11.

[41] W. L. Konijnendijk, and J. M. Stevels. *J Non-Cryst Solids*, **1975**, vol.18, pp. 307-31.

[42] X. F. Lei, and X. X. Xue. *Trans. Nonferrous Met. Soc. China*, **2010**, vol.20, pp. 2294-98.

[43] Y. B. Zong, D. Q. Cang, Y. P. Zhen, Y. Li, and H. Bai. *Trans. Nonferrous Met. Soc. China*, **2009**, vol.19, pp. 834-39.

449 [44] G. Chen, J. Chen, J.H. Peng, and R. D. Wan. *Trans. Nonferrous Met. Soc. China*, **2010**, vol.20,
450 pp. 198-204.
451 [45] D. U. Tulyaganov, S. Agathopoulos, J. M. Ventura, M. A. Karakassides, O. Fabrichnaya, and J.
452 M. F. Ferreira. *J. Eur. Ceram. Soc*, **2006**, vol.26, pp. 1463-71.
453 [46] C. F. Yang, and C. M. Cheng. *Ceram. Int*, **1999**, vol.25, pp. 383-87.
454 [47] W. L. Wang, J. Y. Chen, J. Yu, L. J. Zhou, S. F. Dai, and W. G. Tian. *Waste Management*, **2020**,
455 vol.111, pp. 34-40.
456 [48] V. Shatokha, A. Semykina, J. Nakano, and S. Seetharaman. *J. Min. Metall. Sect. B-Metall*,
457 **2013**, vol.49, pp. 169-74.
458 [49] X. H. Huang, *Metallurgy principle for iron and steel*, third ed., Metallurgical Industry Press,
459 Beijing, 2013.
460 [50] H. L. Fan, H. M. Duan, K. Tan, Y. K. Li, D. F. Chen, M. J. Long, and T. Liu. *JOM*, **2017**,
461 vol.69, pp. 1914-19.
462 [51] H. Agalit, N. Zari, and M. Maaroufi. *Sol. Energy Mater Sol. Cells*, **2017**, vol. 173, pp. 168-76.
463 [52] O. F. Iñigo, C. Nicolas, G. Antoni, J. Rodríguez-Aseguinolaza, A. Faik, and B. D'Aguanno.
464 *Energy*, **2015**, vol.89, pp. 601-09.
465 [53] O. F. Iñigo, G. Yaroslav, O. Ainhoa, P. L. Arias, J. Rodríguez-Aseguinolaza, and A. Faik. *Solar*
466 *Energy*, **2017**, vol.173, pp. 152-59.
467 [54] I. Ortega, A. Faik, A. Gil, J. Rodríguez-Aseguinolaza, and B. D'Aguanno. *Energy Procedia*,
468 **2015**, vol.69, pp. 968-77.
469 [55] J. C. Li, G. X. Li, F. Qiu, R. Wang, J. S. Liang, Y. Zhong, D. Guan, J. W. Li, Z. S. Li, and S.
470 Sridhar. *Int. J. Miner. Metall. Mater.*, **2022**, doi.org/10.1007/s12613-022-2553-x.

471 [56] G. X. Li, J. S. Liang, J. Long, D. Guan, Z. S. Li, S. Sridhar, and J. C. Li. *ISIJ Int.*, **2022**, vol.
472 62, pp. 1556-59.

**Table captions:**

Table I Technical condition of phosphorus recovery of simulated steel slag (Wt.%)

Table II Composition of simulated steel slag (Wt.%)

Table III EDS analysis of different phase areas in the slag 4# at the continuous cooling rate of 10 ℃ /min, corresponding to Figure 6(b) (Wt.%)

Table IV Comparison of precipitated phases for slag 1# and slag 4#

Table V EDS analysis data of the composition of the samples shown in Figure 9

Table VI. Weight fraction (Pct) of phosphorus- and iron-containing phases in the slags

482 Table I. Technical condition of phosphorus recovery of simulated steel slag (Wt.%)

| Researcher | Additive | Amount | Temperature | Slag System |
|---|---|---|---|---|
| Li et al [15] | $SiO_2$ | 10% | 1500 ℃ | $CaO-SiO_2-FeO-Fe_2O_3-P_2O_5$ |
| Jiang et al [16] | $Al_2O_3$ | 11% | 1450 ℃ | $CaO-SiO_2-MgO-MnO-FeO-P_2O_5-Al_2O_3$ |
| Lin et al [17,18] | $SiO_2$; $Al_2O_3$; $TiO_2$ | 10%; 15%; 10% | 1450 ℃ | $CaO-SiO_2-Fe_2O_3-P_2O_5$ |
| Yu et al [19] | $Al_2O_3/TiO_2/Na_2O$ = 15:4:3 | 30% | 1550 ℃ | $CaO-SiO_2-Al_2O_3-Fe_2O_3-P_2O_5$ |
| Li et al [20] | $Na_2O$ | 14% | 1400 ℃ | $CaO-SiO_2-Fe_tO-P_2O_5$ |
| Chen et al [21] | MgO | 9.8% | 1640 ℃ | $CaO-SiO_2-MgO-MnO-FeO-P_2O_5$ |
| Zhang et al [22] | $Al_2O_3$; $TiO_2$ | 11%; 10% | 1350 ℃ | $CaO-SiO_2-MgO-MnO-Fe_tO-P_2O_5$ |

483

484 Table II. Composition of simulated steel slag (Wt.%)

| Slag No. | CaO | $SiO_2$ | FeO | $P_2O_5$ | $B_2O_3$ |
|---|---|---|---|---|---|
| 1# | 38.57 | 15.43 | 36 | 10 | 0 |
| 2# | 37.14 | 14.86 | 36 | 10 | 2 |
| 3# | 35.71 | 14.29 | 36 | 10 | 4 |
| 4# | 34.29 | 13.71 | 36 | 10 | 6 |
| 5# | 32.86 | 13.14 | 36 | 10 | 8 |

485

Table III. EDS analysis of different phase areas in the slag 4# at the continuous cooling rate of 10 ℃/min, corresponding to Figure 6(b) (Wt.%)

| | Ca | Si | O | P | Fe | Potential Formula |
|---|---|---|---|---|---|---|
| Pt1 | 41.87 | 1.25 | 40.01 | 16.87 | -- | $Ca_2PO_{4.8}$ |
| Pt2 | 44.28 | 2.43 | 35.74 | 17.55 | -- | $Ca_2PO_4$ |
| Pt3 | 1.19 | -- | 26.71 | -- | 72.1 | $Fe_3O_{3.9}$ |
| Pt4 | 2.88 | 0.53 | 27.64 | -- | 68.95 | $Fe_3O_{4.2}$ |
| Pt5 | 36.28 | 17.83 | 31.13 | 0.55 | 14.21 | $CaFe_{0.3}Si_{0.7}O_{2.1}$ |
| Pt6 | 35.03 | 18.53 | 29.59 | -- | 16.85 | $CaFe_{0.3}Si_{0.8}O_{2.1}$ |

Note: -- indicates that the elements involved have not been detected due to their relatively tiny amount in the phase area; low X-ray energy boron has not been listed in this table.

489 Table IV. Comparison of precipitated phases for slag 1# and slag 4#

| | **slag 1#** | | **slag 4#** | |
|---|---|---|---|---|
| | 1st crystal phase | 2nd phase phase | 1st crystal phase | 2nd phase phase |
| Morphology | lath-shaped | hexagonally faceted | hexagonally faceted | lath-shaped |
| Temperature of starting precipitation | 1301 ℃ | 1264 ℃ | 1243 ℃ | 1082 ℃ |
| Potential Formula | $Ca_7Si_{3.6}P_{2.5}O_{12}$ (or $Ca_7Si_{3.9}P_{2.4}O_{10.3}$) | $Fe_3O_{4.0}$ (or $Fe_3O_{3.7}$) | $Fe_3O_{3.9}$ (or $Fe_3O_{4.2}$) | $Ca_2PO_{4.8}$ (or $Ca_2PO_4$) |

490

491

492 Table V. EDS analysis data of the composition of the samples shown in Fig.9

| Slag No. | Position | Phases | Ca | Si | O | P | Fe | Potential Formula |
|---|---|---|---|---|---|---|---|---|
| 0# | Pt1 | Fe-rich | 20.61 | 5 | 20.66 | -- | 53.73 | $Ca_2Fe_{3.7}O_{4.8}$ |
| | Pt2 | Matrix | 50.9 | 16.32 | 31.67 | -- | 1.02 | $Ca_2Si_{0.91}O_{3.1}$ |
| | Pt3 | P-rich | 43.26 | 20.06 | 22.33 | 14.35 | -- | $Ca_7Si_{4.67}P_{2.98}O_{9.1}$ |
| 1# | Pt4 | Fe-rich | 3.32 | -- | 26.35 | -- | 70.33 | $Fe_3O_{3.93}$ |
| | Pt5 | Matrix | 50.04 | 15.9 | 33.61 | -- | 0.45 | $Ca_2Si_{0.91}O_{3.4}$ |
| | Pt6 | P-rich | 44.82 | 19.77 | 23.06 | 12.35 | -- | $Ca_7Si_{4.44}P_{2.15}O_{11}$ |
| 2# | Pt7 | Fe-rich | -- | -- | 28.69 | -- | 77.31 | $Fe_3O_{3.89}$ |
| | Pt8 | Matrix | 50 | 15.11 | 33.61 | -- | -- | $Ca_2Si_{0.86}O_{3.36}$ |
| | Pt9 | P-rich | 40.26 | 18.34 | 25.78 | 15.39 | -- | $Ca_7Si_{4.57}P_{3.57}O_{11.2}$ |
| 3# | Pt10 | Fe-rich | -- | -- | 28.4 | -- | 71.6 | $Fe_3O_{4.16}$ |
| | Pt11 | Matrix | 19.76 | 11.67 | 44.97 | -- | 23.6 | $CaFe_{0.85}Si_{0.91}O_{4.25}$ |
| | Pt12 | P-rich | 40.49 | 18.34 | 25.78 | 15.59 | -- | $Ca_7Si_{3.6}P_{3.6}O_{11.2}$ |
| | Pt13 | P-rich | 40.53 | -- | 46.25 | 13.22 | -- | $Ca_3P_{1.31}O_{8.58}$ |
| 4# | Pt14 | Fe-rich | -- | -- | 29.11 | -- | 70.89 | $Fe_3O_{4.3}$ |
| | Pt15 | Matrix | 41.78 | 16.98 | 27.5 | 1.34 | 12.4 | $CaFe_{0.21}Si_{0.58}O_{1.64}$ |
| | Pt16 | P-rich | 49.37 | 0.06 | 34.55 | 16.02 | -- | $Ca_3P_{1.87}O_{7.91}$ |
| 5# | Pt17 | Fe-rich | -- | -- | 32.6 | -- | 67.4 | $Fe_3O_{5.1}$ |
| | Pt18 | Matrix | 20.94 | 11.75 | 46.59 | -- | 20.72 | $CaFe_{0.71}Si_{0.81}O_{5.6}$ |
| | Pt19 | P-rich | 36.64 | -- | 46.84 | 16.52 | -- | $Ca_3P_{1.8}O_{9.56}$ |

Note: -- indicates that the elements involved have not been detected due to their relatively tiny amount in the phase area; low X-ray energy boron has not been listed in this table.

493

494 Table VI. Weight fraction (Pct) of phosphorus- and iron-containing phases in the slags

| **Minerals** | **0#** | **1#** | **2#** | **3#** | **4#** | **5#** |
|---|---|---|---|---|---|---|
| Magnetite ($Fe_3O_4$) | 0 | 38 | 34 | 33 | 31 | 30 |
| $CaFeSi_2O_6$ | 0 | 0 | 18 | 22 | 25 | 28 |
| Solid-solution ($Ca_7Si_2P_2O_{16}$) | 41 | 43 | 29 | 18 | 0 | 0 |
| Calcium phosphate ($Ca_{10}P_6O_{25}$) | 0 | 0 | 0 | 12 | 28 | 25 |

495

**Figure captions:**

**Figure 1.** Schematic diagram of CLSM equipment

**Figure 2.** Change in accumulated amount of different phases precipitated from slags with same composition under different oxygen pressures: (a) 0# (in air); (b) 1# (in high purity argon)

**Figure 3.** Change in accumulated amount of different phases precipitated from slags in Ar atmosphere as a function of $B_2O_3$ addition: (a) 2# - 2% $B_2O_3$; (b) 3# - 4% $B_2O_3$; (c) 4# - 6% $B_2O_3$; (d) 5# - 8% $B_2O_3$

**Figure 4.** Change in the accumulated amount of (a) $Fe_3O_4$ and (b) $Ca_3P_2O_8$ precipitated from different slags

**Figure 5.** Crystallization process of slag 4# in argon at the continuous cooling rate of 10 ℃/min: (a) 1600 ℃; (b) 1243 ℃; (c) 1216 ℃, (d) 1151 ℃; (e) 1082 ℃; (f) 1075 ℃; (g) 1006 ℃; and (h) 917 ℃

**Figure 6.** Morphologies of the crystalline in the slag 4# at continuous cooling rate of 10 ℃/min (a) CLSM image and (b) SEM image

**Figure 7.** EDS map scanning of slag 4# at the continuous cooling rate of 10 ℃/min

**Figure 8.** X-ray diffraction patterns of samples at the continuous cooling rate of 10 ℃/min: (a) Slag 0#; (b) Slag 1#; (c) Slag 2#; (d) Slag 3#; (e) Slag 4#; (f) Slag 5#

**Figure 9.** SEM results of six samples: (a) Slag 0#; (b) Slag 1#; (c) Slag 2#; (d) Slag 3#; (e) Slag 4#; (f) Slag 5#. Slag 0# was cooled in air ($P_{O2}$=0.21 atm) while slags 1# to 5# were cooled in argon ($P_{O2}=10^{-6}$ atm)

**Figure 10.** Phase diagram of CaO-$SiO_2$-FeO-$P_2O_5$ system with the dotted line and dot-dash line corresponding to oxygen partial pressure in air and argon respectively

**Figure 11.** Gibbs free energy change of relevant reactions calculated by FactSage 8.1

**Figure 12.** Schematic diagram of the slag modification